Asymmetric Self-Coherent Detection Based on Mach-Zehnder Interferometers

Xueyang Li, Maurice O'Sullivan, Zhenping Xing, Mohammad E. Mousa-Pasandi, and David V. Plant, *Fellow, IEEE*

***Abstract*—We propose an asymmetric self-coherent detection scheme (ASCD) based on Mach-Zehnder interferometers (MZI) for the field reconstruction of self-coherent (SC) complex double-sideband (DSB) signals. The MZI-ASCD scheme approaches the high electrical spectral efficiency (ESE) of homodyne coherent detection via a direct detection (DD) receiver having only two photodiodes (PD) and two analog-to-digital converters. The incoming SC-DSB signal is split into two parts at the receiver in this approach, one of which is delayed and beats with the other part at the outputs of an MZI. We show that the field reconstruction can be performed from the two tributaries of photocurrents. In addition, we present a modified MZI-ASCD scheme referred to as AUX-ASCD which introduces an auxiliary DD branch to improve the SNR of the detected signal. It is found that both the MZI-ASCD scheme and the AUX-ASCD scheme achieve higher OSNR sensitivity compared to the Kramers-Kronig scheme and in the meantime increases the ESE by a factor of 2 using a cost-effective DD receiver. These advantages make the ASCD scheme attractive for short-reach optical communications including edge cloud connections and mobile X-haul systems.**

***Index Terms*—Coherent detection, intensity modulation direct detection, self-coherent detection, short-reach optical communications.**

I. Introduction

COHERENT detection (COHD) systems revived in the late 2000s due to the rapid development of very-large-scale integration (VLSI) circuits [1]–[4]. Combined with high-speed digital signal processing (DSP), phase-diverse COHD systems allow the digital compensation of various link impairments including chromatic dispersion (CD) and polarization mode dispersion. In addition, COHD systems enable advanced modulation formats with high spectral efficiency and flexible information rate such that the available channel bandwidth can be efficiently utilized. These advantages alongside the ever-increasing demand for higher link capacity result in the wide use of COHD systems in metro and long-haul networks in the last decade [5], [6].

Nevertheless, IMDD systems are still dominant to date in short-reach use cases mainly due to the cost-effectiveness of this approach. However, the data rate-distance product of IMDD systems is constrained by the CD-induced power fading due to a lack of phase information. Recent studies show that the performance of IMDD systems can be enhanced by the DD of self-coherent (SC) single-sideband (SSB) signals. SC-SSB-DD schemes allow the field reconstruction similar to coherent detection while using a cost-effective DD receiver, i.e., a single-ended photodiode (PD). This is achieved by inserting a continuous-wave (CW) tone at the edge of the signal spectrum at the transmitter which generates a tone-signal beating term as part of the photocurrent after detection [7]–[16]. A problem of this approach is the unwanted signal-signal beating interference (SSBI) that can overlap with the baseband signal spectrum. Various techniques have been proposed to mitigate the SSBI in recent years. An earlier approach utilizes a wide guard band to separate the SSBI from the signal at the expense of low electrical spectral efficiency (ESE), defined as the ratio between the system throughput and the receiver electrical bandwidth. Alternatively, by iteratively estimating and removing the SSBI from the photocurrent, the guard band can be significantly narrowed, and higher ESE is achieved [15], [16]. The Kramers-Kronig (KK) detection scheme removes the guard band using a high carrier to signal power ratio (CSPR) in order to satisfy the minimum phase condition [17]–[20]. Another problem of SC-SSB-DD schemes is a more complex transmitter subsystem required to generate SC-SSB signals relative to IMDD systems. Either two digital-to-analog (DAC) channels, a sharp band-rejection filter, or extra RF components [21] are required in SC-SSB-DD systems as opposed to a simpler transmitter in IMDD systems comprised of a single DAC and an intensity modulator. More importantly, the ESE of SC-SSB schemes is only half of that of coherent detection since the image sideband is not encoded with information, and twice the electrical bandwidths are required for the PD and the ADC to detect signals with the same optical bandwidth.

The above limits of SC-SSB-DD schemes prompt the need for schemes that can reconstruct the field of complex double-sideband (DSB) signals based on a DD receiver. SC-DSB-DD schemes approach the transmitter complexity and ESE of coherent detection without a need for a local oscillator (LO). The removal of receiver LOs can lead to reduced power consumption

Manuscript received May 5, 2021; revised August 2, 2021 and November 5, 2021; accepted December 8, 2021. Date of publication December 14, 2021; date of current version April 4, 2022. *(Corresponding author: Xueyang Li.)*

Xueyang Li, Zhenping Xing, and David V. Plant are with the Department of Electrical and Computer Engineering, McGill University, Montreal QC H3A 0E9, Canada (e-mail: xueyang.li@mail.mcgill.ca; zhenping.xing@mail.mcgill.ca; david.plant@mcgill.ca).

Maurice O'Sullivan and Mohammad E. Mousa-Pasandi are with the Ciena Corporation, Ottawa, Ontario K2 K 0L1, Canada (e-mail: mosulliv@ciena.com; mpasandi@ciena.com).

Color versions of one or more figures in this article are available at https://doi.org/10.1109/JLT.2021.3135000.

Digital Object Identifier 10.1109/JLT.2021.3135000

and lower system complexity on several aspects: (a) the remote wavelength management is relaxed, and uncooled lasers could be adopted in coarse wavelength division multiplexing (CWDM) systems, (b) the carrier phase recovery algorithm is eliminated in the DSP, (c) cost-effective lasers with wider linewidth could serve as the optical sources since the impairment due to the phase error is removed. These benefits of SC-DSB-DD schemes are attractive for short-reach optical modems targeting a compact form factor and facing a tight power constraint. As such, several papers on SC-DSB-DD schemes are motivated in recent years [22], [23]. [22] interleaves the CW-tone and signal into staggered time slots at the transmitter and detects the signal by means of a coherent receiver that beats the signal with its delayed copy. Despite the removal of the LO, this scheme does not improve the ESE compared to IMDD because half of the time slots are not carrying signals. In [23], the carrier-assisted differential detection (CADD) scheme is proposed to improve the ESE of [22] close to that of coherent detection using a more complex receiver front-end composed of 5 PDs and three analog-to-digital converters (ADC).

In this paper, we propose an asymmetric self-coherent detection (ASCD) scheme based on Mach-Zehnder interferometers (MZI) for the detection of SC-DSB signals using a cost-effective DD receiver. The incident SC-DSB signal in an MZI-ASCD system is split into two parts, one of which is delayed and beats with the other part when detected at the cross and bar outputs of an MZI. We show that the sum and difference of the two tributaries of photocurrents can be used to reconstruct the signal field. We numerically assess the performance impact of the key system parameters in the MZI-ASCD scheme and extend this scheme to a modified scheme referred to as AUX-ASCD having an auxiliary DD branch used to improve the SNR of the reconstructed signal. Compared to the MZI-ASCD scheme, the AUX-ASCD scheme removes half of the singularities in the spectrum at the cost of an additional PD and thus alleviates the enhancement of the SSBI near 0 GHz. Next, we compare the OSNR sensitivity of different SC detection schemes assuming a CWDM system with a relaxed requirement of laser wavelength stabilization. It is found that both the MZI-ASCD scheme and the AUX-ASCD scheme achieve higher OSNR sensitivity compared to the KK scheme and the CADD scheme. In addition, we perform a practicality analysis to address different problems that can occur during the system implementation and affect the performance of the ASCD schemes.

II. Working Principle

Fig. 1 shows a schematic of a DD receiver having two PDs connected to the output ports of an MZI. The two PDs detect the beatings between the signal portions induced by the MZI which is biased at the intensity quadrature. Note that a power splitter with zero relative phase difference between the output ports is assumed as the front-end of the MZI for the simplicity of the analysis. Due to the physical symmetry of this receiver, the electric signals i_1 and i_2 are identical. More specifically, for an SC-DSB signal expressed as $E(t) = T + s(t)$, where T is the CW-tone, and $s(t)$ is the signal, the sum and difference of the

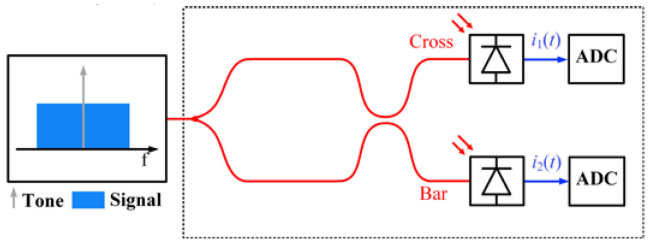

Fig. 1. Schematic of a symmetric DD receiver with an MZI.

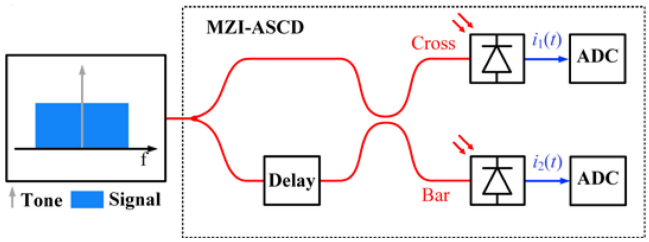

Fig. 2. Schematic of an ASCD receiver.

electric signals are expressed as follows

$$i_1(t)+i_2(t)=\eta|T+s(t)|^2=\eta\left(T^2+2T\mathrm{Re}(s(t))+|s(t)|^2\right), \tag{1}$$

$$i_1(t)-i_2(t)=0, \tag{2}$$

where η is the responsivity of the PD and set to 1 in the following analysis without loss of generality.

We note that this symmetric DD receiver allows the retrieval of only the real part of the complex DSB signal based on (1). In order to reconstruct the full electric field, we break the symmetry of this DD receiver by adding a delay element in one of the MZI branches such that $i_1(t) - i_2(t) \neq 0$, which, as will be shown later, contain additional information for the retrieval of the imaginary part of the signal. We refer to this detection scheme as the MZI-based asymmetric self-coherent detection (ASCD). Fig. 2 shows a schematic of the MZI-ASCD scheme.

The electric signals i_1(t) and i_2(t) can be expressed as follows

$$\begin{aligned} i_1(t) &= \frac{1}{4}|(T+s(t))+j(T+s(t-\tau))|^2 \\ &= \frac{1}{4}\begin{pmatrix} T^2+2T\mathrm{Re}(s(t))+|s(t)|^2 \\ +T^2+2T\mathrm{Re}(s(t-\tau))+|s(t-\tau)|^2 \\ -2\mathrm{Re}((T+s(t))\,j\,(T+s^*(t-\tau))) \end{pmatrix} \end{aligned} \tag{3}$$

$$\begin{aligned} i_2(t) &= \frac{1}{4}|(T+s(t))-j(T+s(t-\tau))|^2 \\ &= \frac{1}{4}\begin{pmatrix} T^2+2T\mathrm{Re}(s(t))+|s(t)|^2 \\ +T^2+2T\mathrm{Re}(s(t-\tau))+|s(t-\tau)|^2 \\ +2\mathrm{Re}((T+s(t))\,j\,(T+s^*(t-\tau))) \end{pmatrix} \end{aligned} \tag{4}$$

where τ represents the delay in the ASCD scheme. Adding i_1(t) and i_2(t) leads to the sum

$$\begin{aligned} & i_1(t)+i_2(t) \\ &= \frac{1}{2}\begin{pmatrix} 2T^2+2T\mathrm{Re}\left(s(t)\right)+2T\mathrm{Re}\left(s(t-\tau)\right) \\ +\left(|s(t)|^2+|s(t-\tau)|^2\right) \end{pmatrix} \\ &= T^2+T\left(s_I(t)+s_I(t-\tau)\right)+u_1(t)+u_1(t-\tau) \end{aligned} \quad (5)$$

where $u_1(t)$ is shorthand for the signal-signal beating interference (SSBI) term $|s(t)|^2/2$. Moreover, the sum of the photocurrents can be used to extract the real part of the signal despite a different form relative to (1). Due to the introduced delay in the MZI, subtracting i_1(t) from i_2(t) leads to a nonzero difference below

$$\begin{aligned} i_1(t)-i_2(t) &= -\mathrm{Re}\left(\left(T+s(t)\right)j\left(T+s^*(t-\tau)\right)\right) \\ &= \mathrm{Im}\begin{pmatrix} T^2+T\left(s(t)+s^*(t-\tau)\right) \\ +s(t)s^*(t-\tau) \end{pmatrix} \\ &= T\left(s_Q(t)-s_Q(t-\tau)\right)+u_2(t) \end{aligned} \quad (6)$$

where $u_2(t)$ is shorthand for the SSBI term $\mathrm{Im}(s(t)s^*(t-\tau))$. Based on (5) and (6), the real and imaginary parts of the signal can be reconstructed in the frequency domain as follows

$$S_I(\omega)=\frac{I_1(\omega)+I_2(\omega)-2\pi T^2\delta(\omega)}{T\left(1+e^{-j\omega\tau}\right)}-\frac{U_1(\omega)}{T} \quad (7)$$

$$S_Q(\omega)=\frac{I_1(\omega)-I_2(\omega)-U_2(\omega)}{T\left(1-e^{-j\omega\tau}\right)} \quad (8)$$

where the Fourier transforms of the terms in the equations are represented in capital letters accordingly. Thus, the field of the signal can be reconstructed based on (7) and (8), i.e., $S(\omega)=S_I(\omega)+jS_Q(\omega)$. Despite our analysis based on a single-polarization configuration, polarization-division-multiplexed MZI-ASCD scheme is achievable by means of a controllable polarization rotator that equalizes the power of the CW-tone at the outputs of a polarization beam splitter using cascaded phase shifters and 2×2 couplers as in [24]–[26]. Alternative approaches include the use of two orthogonal CW-tones separated with a small frequency gap, which is beyond the scope of this paper. It is observed that (7) and (8) contain the transfer functions denoted as $H_I(\omega)=1/(1+\exp(-j\omega\tau))$, and $H_Q(\omega)=1/(1-\exp(-j\omega\tau))$, respectively, which jointly lead to a sequence of equally-spaced singularities at $\omega=k\pi/\tau$ for $S(\omega)$, where k takes all integer numbers. In addition, $H_I(\omega)$ and $H_Q(\omega)$ have different impacts on the SSBI terms contained in the reconstructed real and imaginary part of the signal: the SSBI term $U_1(\omega)$ in $S_I(\omega)$ is not affected by $H_I(\omega)$, whereas the SSBI term $U_2(\omega)$ in $S_Q(\omega)$ is enhanced by the singularities of $H_Q(\omega)$.

Due to the above analysis, the SSBI terms degrade the SNR of the reconstructed signal and should be mitigated in order to improve the performance of the MZI-ASCD scheme. Here we use an iterative feedback algorithm as in [27], [28] to estimate and remove the SSBI terms. We illustrate the principle of the SSBI mitigation algorithm using the schematic diagram shown in Fig. 3. The first reconstruction of $S(\omega)$ is implemented without mitigating the SSBI terms. Note that T can be estimated by use of a short period of zero-valued signal preambles such that the photocurrents are pure DC signals [29]. Then the reconstructed $S(\omega)$ is fed back to obtain an estimate of the SSBI terms, which are subtracted from the sum and difference of the photocurrents. In the second iteration, the reconstructed $S(\omega)$ has improved SNR due to the alleviated SSBI terms. This algorithm can be performed iteratively until the impact of the SSBI is marginal compared to other sources of degradation in the system.

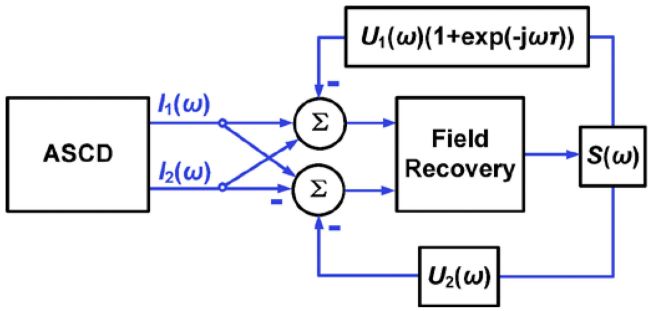

Fig. 3. Iterative SSBI mitigation algorithm.

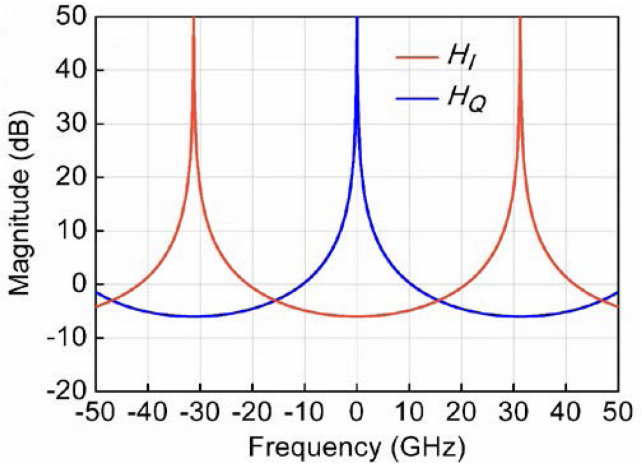

Fig. 4. Magnitude response of H_I and H_Q at a delay of 16 ps.

III. Theoretical Performance Analysis

In this section, we numerically assess the theoretical performance of the MZI-ASCD scheme. Fig. 4 shows the magnitude response of H_I and H_Q in different colors with a 16 ps of delay set in one arm of the MZI. As seen from the figure, the singularities are equally spaced in the spectrum at $\omega=k\pi/\tau$. This indicates that discrete signal bands should be allocated within the spectral intervals partitioned by the singularities in order to avoid significant performance degradation induced by the singularities. The delay in the ASCD system also needs to be optimized to best accommodate the transmitted signal.

We assume a simple signaling scheme in the numerical analysis where the transmitted signal consists of two independent sidebands (ISB), each of which carries a 25 Gbaud 16 QAM

signal. A CW-tone propagates together with the signal over 40 km of single-mode fiber, which is assumed lossless and has a dispersion coefficient of 17 ps/nm/km. Additive white Gaussian noise (AWGN) is linearly added to the optical signal before detection in order to simulate loaded additive spontaneous noise (ASE) for the performance evaluation. To emulate the noise from the PDs and ADCs, a 30 dB electrical noise is added to the downconverted electrical signal based on an electrical signal-to-noise ratio defined as $\langle (s(t) - \langle s(t) \rangle)^2 \rangle / \langle n^2(t) \rangle$, where $\langle x \rangle$ represents the time-domain average of x, $s(t)$ is the electrical signal, and $n(t)$ is the electrical noise. In addition, brick-wall filters are used to simulate the electrical bandwidth of the PDs and ADCs in the receiver, which is configured to pass only the tone-signal beating terms in (3) and (4) while rejecting the out-of-band noise and interferences.

In order to analyze the impact of the SSBI and the noise, we formulate the reconstructed signal based on (7) and (8) as follows without performing iterative SSBI mitigation.

$$S(\omega) + \Delta(\omega) = \begin{pmatrix} \left(I_1(\omega) + I_2(\omega) - 2\pi T^2 \delta(\omega)\right) H_I(\omega)/T \\ +j\left(I_1(\omega) - I_2(\omega)\right) H_Q(\omega)/T \end{pmatrix} \tag{9}$$

$$\Delta(\omega) = \begin{pmatrix} N_{ASE}(\omega) \\ +\left[N_1(\omega) + N_2(\omega)\right] H_I(\omega)/T + U'_1(\omega) \\ +j\left[N_1(\omega) - N_2(\omega) + U'_2(\omega)\right] H_Q(\omega)/T \end{pmatrix} \tag{10}$$

$$U'_1(\omega) = FT\left(|s(t) + n_{ASE}(t)|^2 \Big/ 2\right) \tag{11}$$

$$U'_2(\omega) = FT\left(\mathrm{Im}\left((s(t) + n_{ASE}(t)) \times (s(t-\tau)\, n_{ASE}(t-\tau))^*\right)\right) \tag{12}$$

where $n_{ASE}(t)$, $n_1(t)$, $n_2(t)$ represent the ASE noise, the electrical noise of $i_1(t)$, and the electrical noise of $i_2(t)$, respectively, with the corresponding Fourier transforms denoted as $N_{ASE}(\omega)$, $N_1(\omega)$, and $N_2(\omega)$, respectively. *FT*(*x*) represents the Fourier transmform of x. Thus, it can be seen from (10) that the electrical noises $n_1(t)$, $n_2(t)$ are enhanced by the singularities of $H_I(\omega)$, whereas the electrical noises $n_1(t)$, $n_2(t)$, as well as the SSBI term $U'_2(\omega)$ are all enhanced by the singularities of $H_Q(\omega)$. In order to visualize the impact of the SSBI and the noise, we plot the spectrum of $\Delta(\omega)$ in Fig. 5 with varied delays set in the MZI. It is seen from the figure that the curve corresponding to 16 ps delay has a more pronounced spectral enhancement at 0 GHz relative to the neighboring spectral spikes at ± 31.25 GHz. This is in agreement with (10) because the spectral enhancement near 0 GHz is mainly due to the enhancement of $U'_2(\omega)$ resulting from the 0 GHz singularity of $H_Q(\omega)$, whereas the spectral spikes at $\pm$ 31.25 GHz are caused by the enhancement of the electrical noises due to the singularities of $H_I(\omega)$. At a shorter delay of 10 ps, the frequency interval between the 0 GHz singularity and the neighboring singularities becomes wider, which allows the allocation of signals with higher bandwidth within this interval. We also note stronger spectral enhancement near 0 GHz at

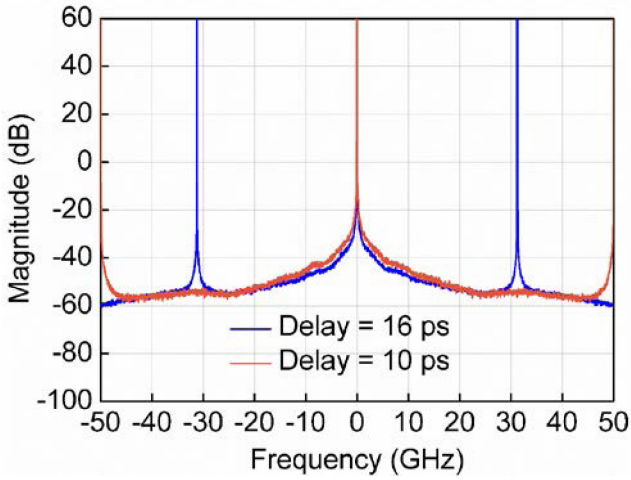

Fig. 5. SSBI spectra at a delay of 10 ps and 16 ps in the MZI.

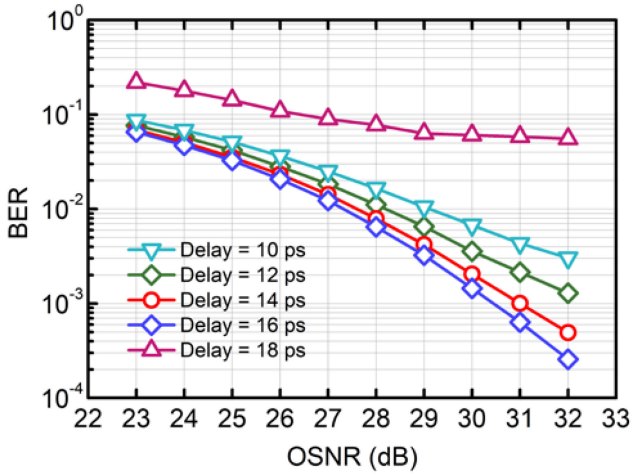

Fig. 6. BER vs. OSNR at a varied delay of 10, 12, 14, 16, and 18 ps.

10 ps compared to 16 ps, which requires a wider guard band in order to alleviate the impact of the spectral enhancement near 0 GHz.

Due to this, we investigate the impact of the delay on the system performance by plotting the BER as a function of OSNR at different delays in the MZI in Fig. 6. The CSPR is set to 9 dB, and the guard band between the edge of the signal sideband and the CW-tone is set to 2 GHz. As seen from the figure, 16 ps delay achieves the lowest BER among all delays. At a higher delay of 18 ps, the singularities of $H_I(\omega)$ corresponding to $k = \pm 1$ are within the signal band. Thus, the BER at 18 ps is significantly higher than the other curves at a lower delay since the performance penalty is mainly due to the enhanced electrical noise caused by the singularities of $H_I(\omega)$. Nevertheless, at a delay lower than 16 ps, the performance also deteriorates because of the stronger enhancement of the SSBI term $U'_2(\omega)$ near 0 GHz as discussed earlier.

Next, we investigate the number of iterations required to mitigate the SSBI terms. Since the algorithms are often

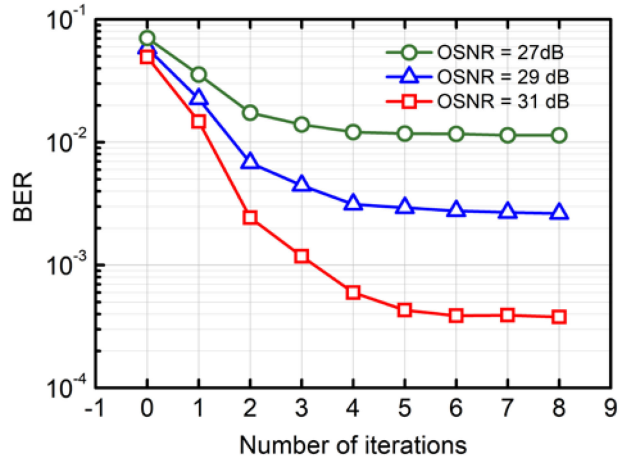

Fig. 7. BER vs. number of iterations at varied OSNRs.

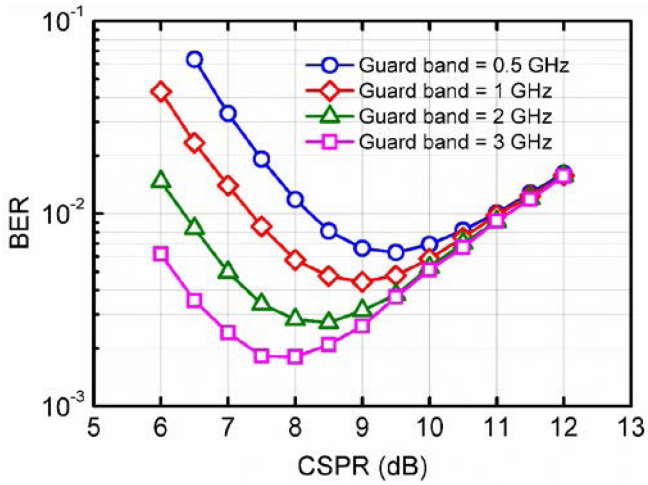

Fig. 9. BER vs. CSPR at varied guard bands.

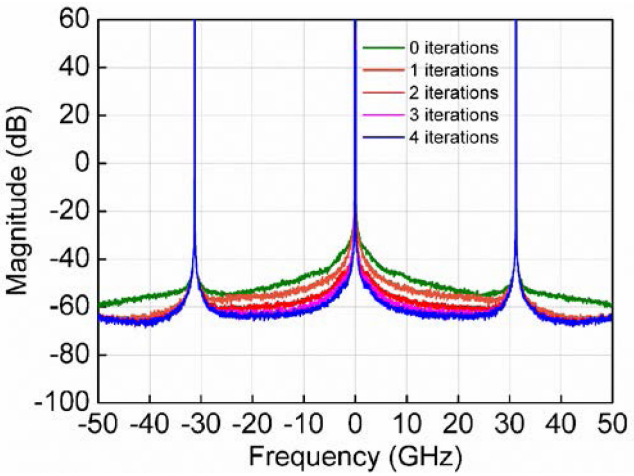

Fig. 8. SSBI spectra at a varied number of iterations.

implemented using pipelined sequential logic circuits for a high circuit throughput, more iterations induce higher circuit latency and require more registers, which gives rise to higher power consumption. Thus, it is desirable to determine the least number of iterations required to effectively mitigate the SSBI. Fig. 7 plots the BER as a function of the number of iterations at varied OSNRs. It can be seen from the figure that the BER decreases with an increasing number of iterations. Moreover, the number of iterations required to attain the BER floor increases as the OSNR increases. The explanation is that at a lower OSNR, the impact of the residual SSBI becomes marginal compared to the noise after fewer iterations, whereas at a higher OSNR, more iterations are needed in order to mitigate the SSBI more completely relative to the noise. As a suitable trade-off between the BER performance and the circuit latency, we use 4 iterations to mitigate the SSBI in the following postprocessing DSP.

At an OSNR of 29 dB, we plot the SSBI spectrum in Fig. 8. The figure shows that as the number of iterations increases, the SSBI terms are mitigated progressively. This is in agreement with the principle of the recursive feedback SSBI mitigation algorithm presented in Section II. In particular, the enhanced SSBI near 0 GHz is significantly suppressed after 4 iterations of SSBI removal, which allows for signal sidebands with a narrower guard band and higher ESE.

Next, we study the performance impact of the CSPR and the guard band at an OSNR of 29 dB. Fig. 9 plots the BER as a function of the CSPR at varied guard bands. The figure shows that the BER decreases and then increases with an increasing CSPR. The minimum BERs of the curves are attained when reaching the optimal trade-off between the effectiveness of the SSBI mitigation and the signal SNR. More specifically, at a lower CSPR, the SSBI estimates based on the reconstructed signal are less accurate due to relatively stronger SSBI enhancement near 0 GHz. On the other hand, the effective signal SNR is lower at a higher CSPR for a given OSNR because the CW-tone is considered as part of the signal in the OSNR calculation. In addition, we observe that the size of the guard band affects the optimal CSPR when achieving the minimum BERs. A lower CSPR is preferred at a wider guard band because the iterative SSBI mitigation is more effective due to weaker SSBI enhancement near 0 GHz and it improves the system performance by having a higher effective SNR. Moreover, as the guard band increases, the BER is significantly reduced.

IV. ASCD With an Auxiliary DD Branch

We show in this section that the performance of the MZI-ASCD scheme can be improved at a slightly higher hardware complexity. Fig. 10 depicts the modified MZI-ASCD scheme. An auxiliary DD branch is introduced to recover the real part of the incident signal and we refer to this modified scheme AUX-ASCD to differentiate it from the MZI-ASCD scheme discussed in Section II. A pair of balanced photodiodes is connected to the output ports of the MZI in order to directly subtract the photocurrents before being sampled by an ADC. Thus, only one extra PD is required in terms of hardware complexity compared to the MZI-ASCD scheme.

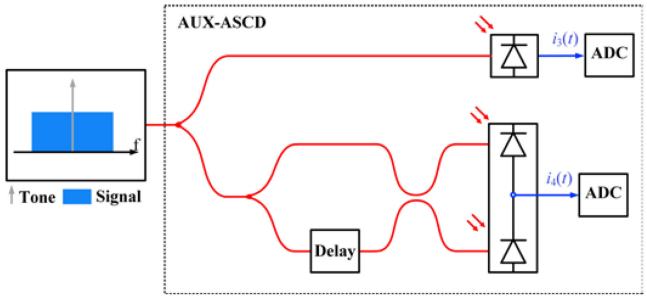

Fig. 10. Schematic of the ASCD scheme with an auxiliary DD branch.

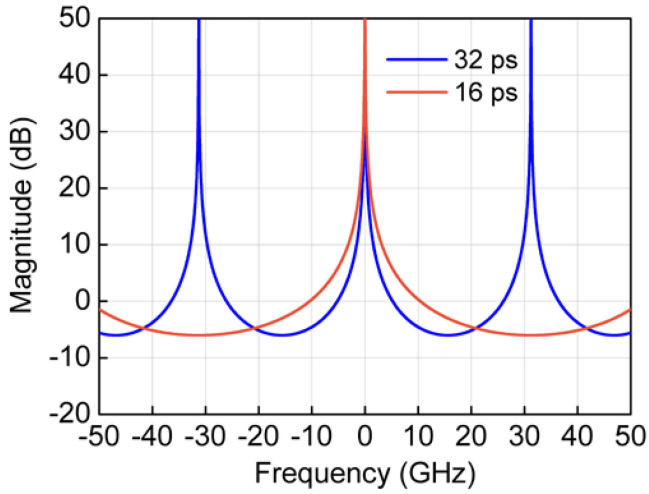

Fig. 11. Magnitude response of H_Q at 16 ps and 32 ps of delay.

The photocurrents i_3(t) and i_4(t) can be expressed as

$$i_3(t) = \frac{1}{2}\left(T^2 + 2Ts_I(t) + |s(t)|^2\right) = \frac{1}{2}T^2 + Ts_I(t) + u_1(t) \quad (13)$$

$$i_4(t) = \frac{1}{2}\left[i_1(t) - i_2(t)\right] \quad (14)$$

Thus, the imaginary and real parts of the signal can be expressed as follows

$$S_I(\omega) = \frac{I_3(\omega) - U_1(\omega)}{T} - \pi T\delta(\omega) \quad (15)$$

$$S_Q(\omega) = \frac{2I_4(\omega) - U_2(\omega)}{T\left(1 - e^{-j\omega\tau}\right)} \quad (16)$$

The major difference of the field reconstruction based on (15) and (16) compared to that based on (7) and (8) is the elimination of the transfer function H_I. Thus, the singularities of the AUX-ASCD scheme are distributed at $\omega = 2k\pi/\tau$, which increases the spacing between the singularities by a factor of 2 at a given delay. Consequently, the optimal delay for the same 16 QAM signal at 50 Gbaud is 32 ps for the AUX-ASCD scheme, which is two times the optimal delay of 16 ps for the MZI-ASCD scheme. Fig. 11 compares the transfer function H_Q at 16 ps and 32 ps delay, respectively. It follows that stronger SSBI enhancement

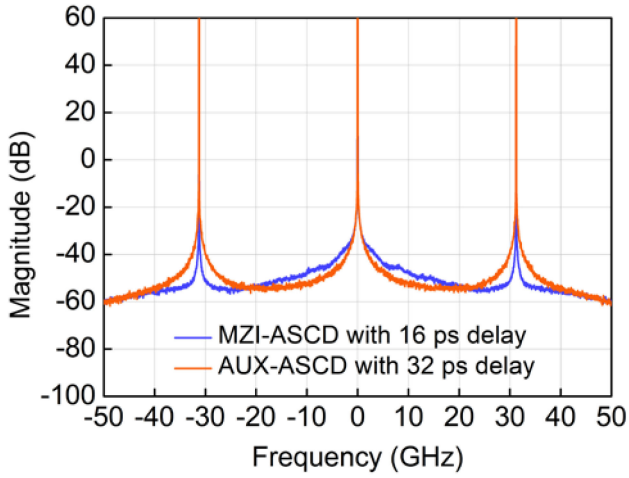

Fig. 12. SSBI spectra after a first signal field reconstruction for the MZI-ASCD scheme and the AUX-ASCD scheme at 16 ps and 32 ps delay, respectively.

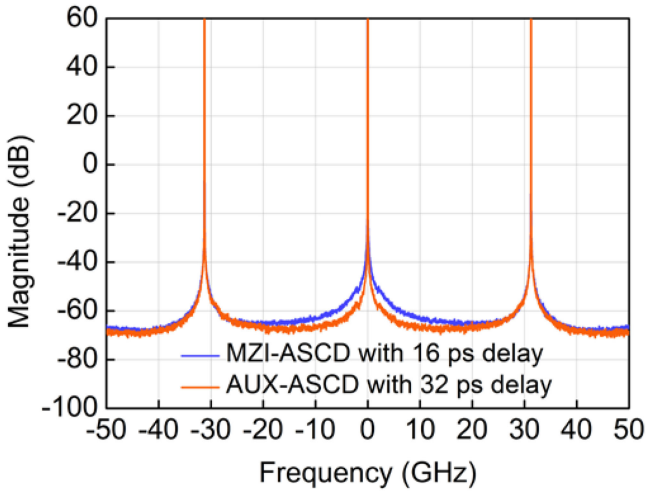

Fig. 13. Spectra of the residual SSBI after 4 iterations of SSBI cancellation for the MZI-ASCD scheme and the AUX-ASCD scheme at 16 ps and 32 ps delay, respectively.

near 0 GHz should be induced by H_Q at 16 ps of delay compared to H_Q at 32 ps of delay.

To verify this, we compare the enhanced SSBI between the MZI-ASCD scheme and the AUX-ASCD scheme without SSBI mitigation in Fig. 12. It is seen in the figure that the AUX-ASCD scheme has weaker SSBI enhancement near 0 GHz as expected from the transfer function plotted in Fig. 11. However, the spectral enhancement around 31.25 GHz is stronger for the AUX-ASCD scheme since H_I associated with the MZI-ASCD scheme does not enhance the SSBI.

We also compare the spectrum of the residual SSBI after 4 iterations of SSBI cancellation in Fig. 13. As seen in the figure, the residual SSBI near 0 GHz is still stronger for the MZI-ASCD scheme compared to the AUX-ASCD scheme due to H_Q at a lower delay of 16 ps. However, the residual SSBIs are similar around the singularities of ± 31.25 GHz for both schemes after SSBI mitigation. The figure indicates that the

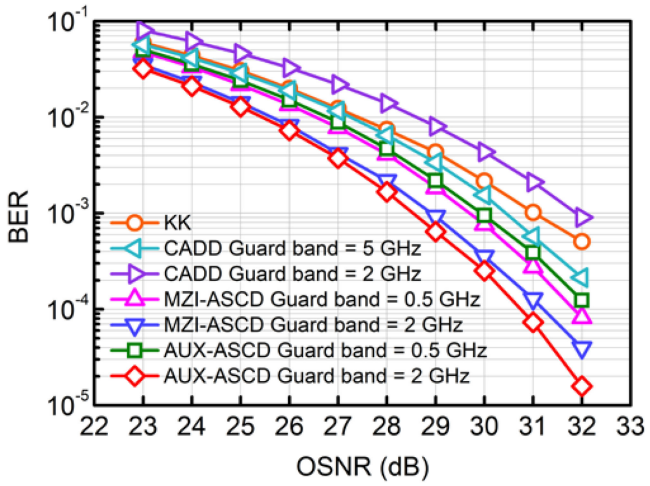

Fig. 14. OSNR sensitivity for different detection schemes.

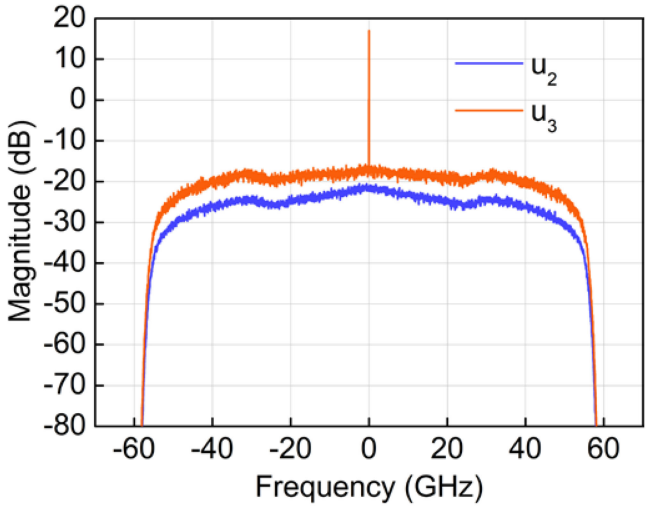

Fig. 15. Spectra of the SSBI terms $u_2(t)$ and $u_3(t)$.

AUX-ASCD scheme can achieve better performance compared to the MZI-ASCD scheme due to weaker residual SSBI within the interval for the signal allocation.

V. OSNR Sensitivity Comparison

In this section, we compare the OSNR sensitivity of different self-coherent detection schemes in the back-to-back configuration (B2B). Fig. 14 plots the BER as a function of the OSNR for the MZI-ASCD scheme, the ASCD-AUX scheme, and the CADD scheme at varied guard bands with optimized delays to accommodate the signal. 4 iterations of SSBI mitigation are implemented for these SC-DSB-DD schemes. Note that the SSBI estimates are obtained from the reconstructed signal field as detailed in section II, which is different from the approach adopted in [23] where the SSBI estimates are based on clean symbols determined after equalization at the expense of higher complexity. In addition, we include the OSNR sensitivity of the KK scheme in this figure. For a fair comparison, we transmit a 50 Gbaud single-sideband 16 QAM signal in the KK scheme and an aggregate 50 Gbaud dual-sideband 16 QAM signal in the ASCD schemes, and the CADD scheme. Due to the spectral expansion induced by nonlinear operations used in the KK scheme, a relatively higher sampling rate of 200 GSa/s is set for the KK scheme, whereas a lower sampling rate of 100 GSa/s is set for the SC-DSB-DD schemes. In addition, brick-wall filters are used to simulate the electrical bandwidth of the PDs and ADCs and are configured to pass only the tone-signal beating term in all schemes considered. This configuration of the electrical bandwidth leads to rejection of the out-of-band SSBI for the ASCD and CADD schemes. Nevertheless, since a specific relation between the signal and the SSBI is not required by these two schemes to perform signal reconstruction, the signal SNR is not degraded due to the removal of part of the SSBI. For the KK scheme, the SSBI bandwidth is as wide as the tone-signal beating term and thus not rejected. Note that no electrical noise is added at the receiver in the OSNR sensitivity analysis. Since the CSPR affects the iterative SSBI cancellation and the effective OSNR which excludes the contribution of the carrier, the CSPR is optimized at each OSNR due to a different level of ASE noise [30]. In order to relax the requirement for the remote wavelength management and even allow the use of uncooled lasers, we assume no use of extra filters to reject the out-of-band ASE noise for optical signals from a CWDM demux having a wide passband. Thus, the ASE noise in the image sideband as wide as the signal sideband is considered for SC-SSB signals, whereas only in-band ASE noise is considered for SC-DSB signals in the simulation.

The figure shows that the ASCD schemes and the CADD scheme can achieve lower BER compared to the KK scheme at sufficiently wide guard bands used to effectively mitigate the enhanced SSBI near 0 GHz. The worse OSNR sensitivity of the KK scheme is due to the ASE noise from the image sideband that beats with the CW-tone after detection, thus resulting in degraded SNR of the baseband signal [31]. We also note that the SC-DSB-DD schemes discussed here require approximately half of the electrical bandwidth relative to the KK scheme. At the same guard band of 2 GHz, it is observed that both ASCD schemes achieve significantly lower BER compared to the CADD scheme. The explanation is that the power of the SSBI term $u_3(t) = s(t)s^*(t-\tau) - |s(t-\tau)|^2$ in the CADD scheme [23] is stronger compared to $u_2(t) = \mathrm{Im}(s(t)s^*(t-\tau))$ in the ASCD schemes, which can be visualized from the spectra of these two SSBI terms in Fig. 15. Since $u_2(t)$ and $u_3(t)$ are enhanced by the same transfer function $H_Q(\omega)$ near 0 GHz, the residual SSBI in the CADD scheme is more pronounced after the iterative SSBI cancellation and leads to lower OSNR sensitivity when the same guard band is used. It is also found that the AUX-ASCD scheme performs slightly better than the MZI-ASCD scheme, achieving the lowest BER among the three SC-DSB-DD schemes. In terms of the hardware complexity, the AUX-ASCD scheme eliminates the use of two extra PDs and one ADC compared to the CADD scheme but requires one more PD compared to the MZI-ASCD scheme.

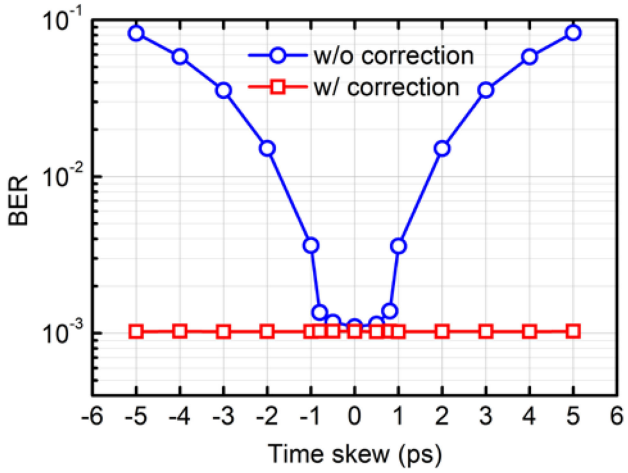

Fig. 16. BER versus the time skew with and without digital skew correction.

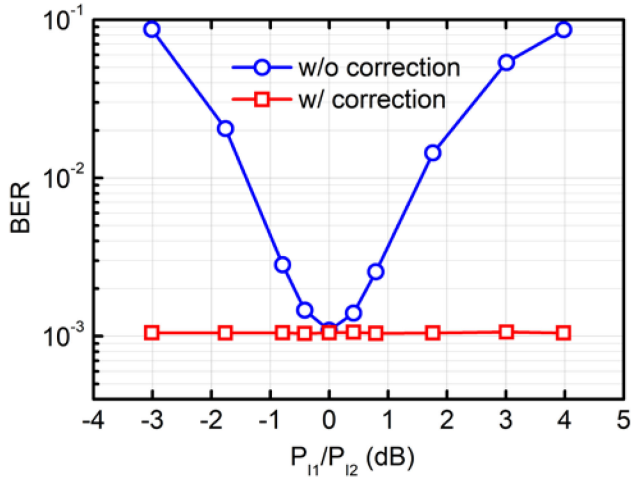

Fig. 17. BER versus the power ratio between $i_1(t)$ and $i_2(t)$ in dB.

VI. Practicality Analysis

In this section, we evaluate the performance impact of various problems that can occur during the actual implementation of the ASCD schemes. Since the AUX-ASCD scheme is extended from the MZI-ASCD scheme sharing a similar MZI structure, we focus on the MZI-ASCD scheme here and a similar analysis can be carried out for the AUX-ASCD scheme. In the analysis, the MZI-ASCD system is in the B2B configuration with 8 dB CSPR and 29 dB OSNR. A dual-sideband 16 QAM signal with a 50 Gbaud aggregate symbol rate and a 2 GHz guard band per sideband is detected in the MZI-ASCD system.

As discussed in section II, the signal reconstruction of the MZI-ASCD scheme is based on the sum and difference of the photocurrents $i_1(t)$ and $i_2(t)$. Though a zero time skew is assumed in the derivation, the misalignment of the photocurrents in the time domain due to the receiver hardware can lead to deteriorated system performance. We show as follows that the time skew can be estimated at back-to-back and corrected digitally in the receiver DSP. The skew estimation is realized by use of a sequence of synchronization symbols, which are loaded with only the in-phase component of the signal, i.e., $s_I(t)$. Based on (3) and (4), it is found that $i_1(t)$ equals $i_2(t)$ when $s_Q(t)$ is removed from $s(t)$. The photocurrents are expressed as follows:

$$\begin{aligned} i_1(t) &= i_2(t) \\ &= \frac{1}{4}\Big(2T^2 + 2T\left(s_I(t) + s_I(t-\tau)\right) \\ &\quad + |s_I(t)|^2 + |s_I(t-\tau)|^2\Big) \end{aligned} \tag{17}$$

Thus, the time skew can be readily estimated based on the cross-correlation of $i_1(t)$ and $i_2(t)$. Fig. 16 plots the change of the BER versus the time skew μ applied to $i_2(t)$, i.e., $i_2(t-\mu)$. It is seen from the figure that the BER increases significantly when the absolute time skew is greater than 1 ps. After correcting the time skew using the proposed method, the associated performance penalty is eliminated.

In addition, we also investigate the performance penalty due to the imbalanced amplitudes of the photocurrents. Fig. 17 plots the change of the BER as a function of the power ratio between $i_1(t)$ and $i_2(t)$ in dB. A significant BER increase is observed in the figure as the amplitude imbalance of the photocurrents becomes more severe. We note that the BER grows beyond 1×10^{-2} when the power ratio P_{I1}/P_{I2} is less than -2 dB or greater than 2 dB. This amplitude imbalance can be corrected by equalizing the average power of $i_1(t)$ and $i_2(t)$. As shown in the figure, the performance of the MZI-ASCD scheme is no longer affected by the amplitude imbalance of the photocurrents with correction.

Due to reasons including fabrication errors or temperature variation, the delay in the MZI can deviate from the desired value and drift over time. Thus, it is important to estimate the actual delay for the subsequent signal reconstruction DSP. After correcting the time skew and the amplitude imbalance of the photocurrents as discussed earlier, we can observe multiple notches from the amplitude response of $i_1(t) + i_2(t)$, which is due to the transfer function $H_I(\omega)$ based on (5). Since the location of the notches is uniquely determined by $H_I(\omega)$ and therefore τ, the delay can be estimated accordingly based on the size of the frequency interval between neighboring notches. Fig. 18 plots the estimated delay versus the actual delay in the MZI. As a reference, the function $y = x$ is also plotted in the figure. We can see from this figure that the delay estimates lie on the dashed line, showing a good estimation accuracy of this approach.

Next, we characterize in Fig. 19 the BER of the signal reconstructed using the estimated delay and the actual delay, respectively. It is observed from the figure that the two curves overlap with each other due to accurate delay estimates. Moreover, it is found that the BER reaches the minimum at 16 ps and increases sharply at a higher delay in the MZI since the singularities corresponding to $k = \pm 1$ of $H_I(\omega)$ move within the signal band. This is in agreement with our earlier discussion about Fig. 5. By contrast, the BER increases relatively slowly as

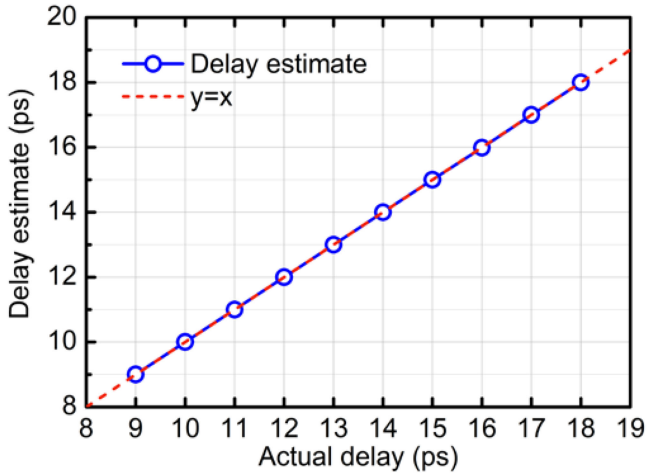

Fig. 18. Delay estimates at given delays in the MZI.

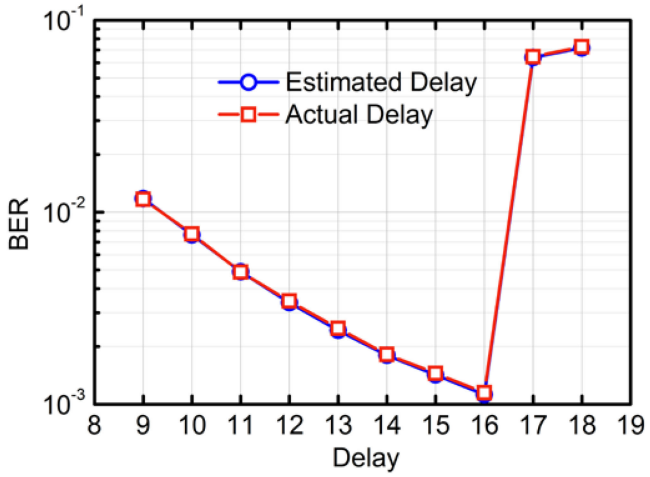

Fig. 19. BER versus the delay in the MZI for the reconstructed signal based on the estimated delay and the actual delay, respectively.

the delay decreases from 16 ps to 9 ps. This indicates that it is practical to set the delay to around 12 ps in this case in order to allow a greater margin to accommodate the potential fluctuation of the delay despite a relatively higher BER

VII. Conclusion

We propose in this paper a cost-effective DD scheme for SC-DSB signals using two PDs and two ADCs. We derive the equations to reconstructing the field of the DSB signal from the outputs of an MZI that beats a portion of the signal with the other portion delayed by τ. We analyze the effect of SSBI enhancement due to the transfer function singularities associated with the MZI-ASCD scheme and discuss appropriate signaling schemes to allocate the signal bands within the spectral intervals. A numerical analysis follows to evaluate the theoretical performance of the MZI-ASCD scheme by loading ASE-noise. In addition, a modified ASCD scheme termed AUX-ASCD is derived from the MZI-ASCD scheme, which improves the SNR of the detected signal relative to the MZI-ASCD scheme by alleviating the SSBI enhancement at the expense of an additional PD. Next, we compare the OSNR sensitivity of different detection schemes in the B2B configuration. The results show that both ASCD schemes achieve better OSNR sensitivity compared to the KK scheme and the CADD scheme with the AUX-ASCD scheme slightly outperforming the MZI-ASCD scheme. We also assess the impact of various implementation problems and show the effectiveness of digital algorithms in compensating for the corresponding performance penalty. To summarize, the ASCD schemes combine a high ESE approaching that of coherent detection with the cost-effectiveness of DD, thus holding promise for high-speed short-reach communications including the interconnects between edge cloud data centers and mobile X-haul systems.

References

[1] K. Zhong, X. Zhou, J. Huo, C. Yu, C. Lu, and A. P. Tao Lau, "Digital signal processing for short-reach optical communications: A review of current technologies and future trends," *J. Lightw. Technol.*, vol. 36, no. 2, pp. 377–400, Jan. 2018.

[2] P. J. Winzer *et al.*, "Advanced optical modulation formats," in *Optical Fiber Telecommunications VB*, I. Kaminow and T. Li, Eds. New York, NY, USA: Academic, 2008, pp. 232–304.

[3] S. J. Savory *et al.*, "Electronic compensation of chromatic dispersion using a digital coherent receiver," *Opt. Express*, vol. 15, pp. 2120–2126, 2007.

[4] E. M. Ip and J. M. Kahn, "Fiber impairment compensation using coherent detection and digital signal processing," *J. Lightw. Technol.*, vol. 28, no. 4, pp. 502–519, Feb. 2010.

[5] F. Buchali *et al.*, "1.52 Tb/s single carrier transmission supported by a 128 GSa/s SiGe DAC," in *Proc. Opt. Fiber Commun. Conf.*, 2020, Paper Th4C.2.

[6] M. Schuster *et al.*, "Spectrally efficient compatible single-sideband modulation for OFDM transmission with direct detection," *IEEE Photon. Technol. Lett.*, vol. 20, no. 9, pp. 670–672, May 2008.

[7] S. Randel *et al.*, "100-Gb/s discrete-multitone transmission over 80-km SSMF using single-sideband modulation with novel interference-cancellation scheme," in *Proc. Eur. Conf. Opt. Commun.*, Valencia, Spain, 2015, pp. 1–3.

[8] X. Liu *et al.*, "Digital self-coherent detection," *Opt. Express*, vol. 16, pp. 792–803, 2008.

[9] D. Che, Q. Hu, and W. Shieh, "Linearization of direct detection optical channels using self-coherent subsystems," *J. Lightw. Technol.*, vol. 34, no. 2, pp. 516–524, Jan. 2016.

[10] D. Che, C. Sun, and W. Shieh, "Optical field recovery in stokes space," *J. Lightw. Technol.*, vol. 37, no. 2, pp. 451–460, Jan. 2019.

[11] X. Chen *et al.*, "218-Gb/s single-wavelength, single-polarization, single-photodiode transmission over 125-km of standard singlemode fiber using Kramers-Kronig detection," in *Opt. Fiber Commun. Conf. Postdeadline Papers, OSA Tech. Dig. (Online)*, 2017, Paper Th5B.6.

[12] S. T. Le *et al.*, "1.72-Tb/s Virtual-Carrier-Assisted direct-detection transmission over 200 km," *J. Lightw. Technol.*, vol. 36, no. 6, pp. 1347–1353, Mar. 2018.

[13] B. J. C. Schmidt, A. J. Lowery, and J. Armstrong, "Experimental demonstrations of electronic dispersion compensation for long-haul transmission using direct-detection optical OFDM," *J. Lightw. Technol.*, vol. 26, no. 1, pp. 196–203, Jan. 2008.

[14] W. R. Peng *et al.*, "Spectrally efficient direct-detected OFDM transmission employing an iterative estimation and cancellation technique," *Opt. Express*, vol. 17, pp. 9099–9111, 2009.

[15] Z. Li *et al.*, "SSBI mitigation and the Kramers–Kronig scheme in single-sideband direct-detection transmission with receiver-based electronic dispersion compensation," *J. Lightw. Technol.*, vol. 35, no. 10, pp. 1887–1893, May 2017.

[16] Z. Xing *et al.*, "100 Gb/s PAM4 transmission system for datacenter interconnects using a SiP ME-MZM based DAC-less transmitter and a VSB self-coherent receiver," *Opt. Express*, vol. 26, no. 18, pp. 23969–23979, Sep. 2018.

[17] A. Mecozzi *et al.*, *Adv. Opt. Photon.*, vol. 11, pp. 480–517, 2019.

[18] A. Mecozzi *et al.*, *Optica*, vol. 3, pp. 1220–1227, 2016.
[19] X. Chen *et al.*, "Kramers–Kronig receivers for 100-km datacenter interconnects," *J. Lightw. Technol.*, vol. 36, no. 1, pp. 79–89, Jan. 2018.
[20] T. Bo *et al.*, "Kramers-Kronig receiver operable without digital upsampling," *Opt. Express*, vol. 26, pp. 13810–13818, 2018.
[21] X. Li, M. S. Alam, M. E. Mousa-Pasandi, M. O'Sullivan, and D. V. Plant, "Demonstration of C-band amplifier-free 100 Gb/s/λ direct-detection links beyond 40-km SMF using a high-power SSB transmitter," *J. Lightw. Technol.*, vol. 38, no. 22, pp. 6170–6177, Nov. 2020.
[22] X. Chen *et al.*, "Signal-carrier interleaved optical OFDM for direct detection optical communication," *Opt. Express*, vol. 21, pp. 32501–32507, 2013.
[23] W. Shieh *et al.*, "Carrier-assisted differential detection," *Light Sci. Appl.*, vol. 9, no. 18, 2020, https://doi.org/10.1038/s41377-020-0253-8
[24] T. Gui, X. Wang, M. Tang, Y. Yu, Y. Lu, and L. Li, "Real-Time demonstration of homodyne coherent bidirectional transmission for next-generation data center interconnects," *J. Lightw. Technol.*, vol. 39, no. 4, pp. 1231–1238, Feb. 2021.
[25] A. Nespola *et al.*, "Proof of concept of polarization-multiplexed PAM using a compact Si-Ph device," *IEEE Photon. Technol. Lett.*, vol. 31, no. 1, pp. 62–65, Jan. 2019.
[26] C. K. Madsen *et al.*, "Reset-free integrated polarization controller using phase shifters," *IEEE J. Sel. Topics Quantum Electron.*, vol. 11, no. 2, pp. 431–438, Mar. 2005.
[27] X. Li *et al.*, "Asymmetric direct detection of twin-SSB signals," *Opt. Lett.*, vol. 45, pp. 844–847, 2020.
[28] X. Li *et al.*, "Asymmetric self-coherent detection," *Opt. Express*, vol. 29, pp. 25412–25427, 2021.
[29] T. Bo *et al.*, "Recovery of DC component in kramers-kronig receiver utilizing AC-coupled photo-detector," in *Proc. Opt. Fiber Commun. Conf., OSA Tech. Dig.*, 2020, Paper M3J.1.
[30] C. Sun, D. Che, H. Ji, and W. Shieh, "Study of chromatic dispersion impacts on Kramers–Kronig and SSBI iterative cancellation receiver," *IEEE Photon. Technol. Lett* ., vol. 31, no. 4, pp. 303–306, Feb. 2019.
[31] X. Chen *et al.*, in *Proc. Eur. Conf. Opt. Commun.*, 2018, pp. 1–3, doi: 10.1109/ECOC.2018.8535234.